

condensate. The dependence of the energy of these states on the magnetic field is plotted in Fig. 4 (top). One could predict that such states are due to different numbers of Abrikosov vortices that can fit into a small volume. The situation resembles magnetization peaks observed in layered superconductors as the result of varying numbers of vortex rows in the sample<sup>7,8</sup>. The initial stages of magnetization in mesoscopic superconductors were also described as evolution along different vortex phases in recent theoretical works, using a semi-classical model of interacting vortices<sup>9,10</sup>. We have obtained a better and more complete description of the experimental data by numerically solving the nonlinear GL equations<sup>1,8</sup>; the results are shown in Fig. 4. The quantum states clearly correspond to integral numbers  $N$  of Abrikosov vortices (Fig. 4, insets). The different curves  $\Delta F(H)$  are shifted along the horizontal axis by  $\Delta H \approx \phi_0/s$ , indicating one-by-one entries of vortex cores inside the disk area  $s$ . Note that although the number of vortices in the sample is quantized, there is no quantization of the magnetic flux because some of it 'spills out' of the sample owing to the presence of the boundary. This also leads to smooth penetration of the magnetic field inside the superconductor (nonlinear Meissner effect), which can be seen as the rounding of the upper parts of the curves in Figs 2 and 4.

Although the presence of the sample boundary explains the non-quantized flux jumps qualitatively, neither of the existing theories predicts the possibility of fractional jumps (much smaller than  $\phi_0$ ) observed in our largest, multi-flux-quanta superconductors in high fields. We attribute them to changes in the vortex configurations for a constant number of vortices inside the superconductor. Indeed, our numerical simulations of the GL equations find multiple stable vortex configurations for  $N \geq 5$  (vortex configurations are also discussed in refs 8, 10). Different configurations assume different energies and lead to different amounts of magnetic flux spilling out. Therefore, transitions between such states occur with minor flux jumps. The number of possible vortex configurations increases with increasing  $N$ , which can explain the jumps getting smaller with increasing field. It is also possible that shape irregularities allow additional vortex configurations.

Finally, there is a clear analogy between our work and current intensive studies of electron spectra in confined geometries, commonly referred to as quantum dots or artificial atoms (reviewed in ref. 11). In fact, the GL equations can be seen physically as a Schrödinger-type equation for the centre-of-mass motion of Cooper pairs (with strong non-local interaction via vector potential)<sup>1</sup>. From this viewpoint, mesoscopic superconductors present "artificial atoms made from Cooper pairs rather than electrons" and we can equally interpret Figs 3 and 4 in terms of energy spectra of non-interacting and interacting Cooper pairs, respectively. □

Received 8 May; accepted 23 September 1997.

- de Gennes, P. G. *Superconductivity in Metals and Alloys* (Addison-Wesley, New York, 1989).
- Parks, R. D. & Little, W. A. Fluxoid quantization in a multiply-connected superconductor. *Phys. Rev. A* **133**, 97–103 (1964).
- Buisson, O., Gandit, P., Rammal, R., Wang, Y. Y. & Pannetier, B. Magnetization oscillations of a superconducting disk. *Phys. Lett. A* **150**, 36–42 (1990).
- Moshchalkov, V. V. *et al.* Effect of sample topology on the critical fields of mesoscopic superconductors. *Nature* **373**, 319–322 (1995).
- Geim, A. K. *et al.* Ballistic Hall micromagnetometry. *Appl. Phys. Lett.* **71**, 2379–2381 (1997).
- Black, C. T., Ralph, D. C. & Tinkham, M. Spectroscopy of the superconducting gap in individual nanometer-scale aluminum particles. *Phys. Rev. Lett.* **76**, 688–691 (1996).
- Brongersma, S. H., Verweij, E., Koeman, N. J., de Groot, D. G. & Griessen, R. Series of maxima in the field dependent magnetic moment of layered superconductors. *Phys. Rev. Lett.* **71**, 2319–2322 (1993).
- Bolech, A. C., Buscaglia, G. C. & Lopez, A. Numerical simulation of vortex arrays in thin superconducting films. *Phys. Rev. B* **52**, 15719–15722 (1995).
- Buzdin, A. I. & Brison, J. P. Vortex structures in small superconducting disks. *Phys. Lett. A* **196**, 267–271 (1994).
- Krasilnikov, A. S., Mamsurova, L. G., Trusevich, N. G., Shcherbakova, L. G. & Pukhov, K. K. Fine-grained YBaCuO: the formation of the initial vortex lattice and the magnetization curves. *Supercond. Sci. Technol.* **8**, 1–5 (1995).
- Ashoori, R. C. Electrons in artificial atoms. *Nature* **379**, 413–419 (1996).

**Acknowledgements.** We thank INTAS, FOM and NATO for financial support.

Correspondence and requests for materials should be addressed to A.K.G. (e-mail: geim@sci.kun.nl).

## Giant fluctuations in a free diffusion process

Alberto Vailati & Marzio Giglio

Dipartimento di Fisica and Istituto Nazionale per la Fisica della Materia, Università di Milano, via Celoria 16, 20133 Milano, Italy

Macroscopic concentration gradients in physical systems relax towards equilibrium by diffusion<sup>1–3</sup>, in the absence of bulk motion. This is normally regarded as a spatially homogeneous mixing process. Here, however, we show that unexpectedly large spatial fluctuations in concentration can occur during a free diffusion process. We set up an initially sharp interface between two miscible fluids by letting a mixture phase-separate below the critical consolution temperature and then raising the temperature quickly to the single-phase region. Shadowgraph images and low-angle light scattering show evidence for large fluctuations in composition, orders of magnitude larger in amplitude than those seen in the equilibrium state. We show that these pronounced inhomogeneities are due to a coupling between velocity

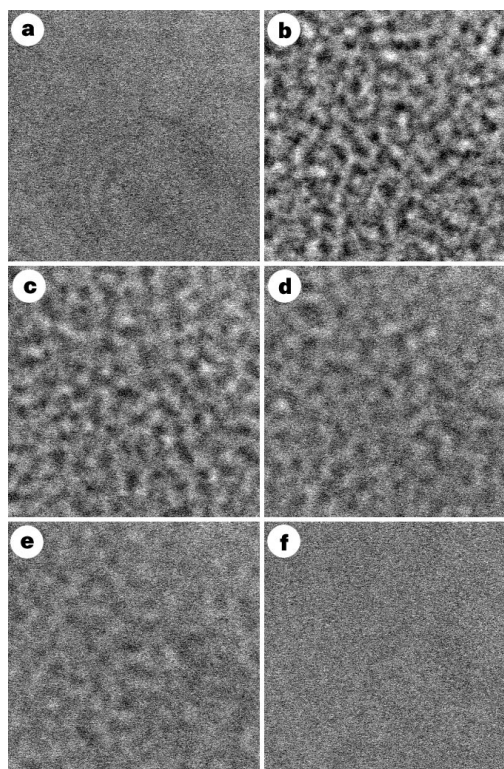


**Figure 1** Shadowgraph images of the sample during the diffusion process. The images were generated by shining a vertical white-light beam on an horizontal layer of sample and by imaging the sample slightly out of focus on a CCD (charge-coupled device) camera. Image **a** was acquired when the sample was kept below its critical temperature  $T_c$ , where the sample consists of two layers of immiscible fluids separated by a sharp interface, and no diffusion occurs. A temperature jump was then applied to bring the sample above  $T_c$ , where the two layers become miscible, and the diffusion process started. The images **b–f** were taken at different times after the application of the temperature jump: **b**, 100 s; **c**, 9 min; **d**, 90 min; **e**, 330 min; and **f**, 3 days. To get rid of non-uniform illumination, the images were processed by subtracting a reference image acquired when the sample was homogeneous. The side of each image is 1 mm in real space.

and concentration fluctuations in the non-equilibrium state<sup>4-6</sup>. Gravity cuts off the fluctuations above a certain wavelength, and the amplitude of the fluctuations at longer wavelengths does not depend on any relevant thermodynamic property of the fluid. As a consequence, these giant fluctuations should be observable in any mixture undergoing mixing by diffusion.

In an ideal free diffusion experiment, two samples of miscible fluids at different concentrations are separated by a sharp, flat surface at time  $t = 0$ . A measurement of the time evolution of the concentration profiles readily gives an estimate of the diffusion coefficient<sup>1,2</sup>. To avoid difficulties in the preparation of the initial sharp boundary we have chosen a liquid mixture not far from a consolution critical point (aniline and cyclohexane), the concentration being very close to the critical one<sup>7</sup>. The sample is first brought to a temperature  $T$  below the critical point ( $T_c - T = 3$  K), so that it separates into two phases with a mass fraction concentration difference<sup>8</sup>  $\delta c = 0.5$ , and a sharp horizontal interface is formed at the mid-height of the cell. The temperature is then rapidly brought above the critical temperature at  $T - T_c = 1.0$  K. The thermal time constant is of the order of one minute, to be compared with the mass diffusion constant, which is of the order of a few hours. The large difference in the time constants is partly a consequence of working close to a critical point, as diffusion is (in our conditions) a factor of ten slower than in ordinary liquid mixtures. It must be stressed that once the new temperature above  $T_c$  has been reached, there is no phase transition to speak of, as we are dealing now with an isothermal system above  $T_c$ , which happens to be in a spatially inhomogeneous state and hence has to go back to the homogeneous state via diffusion (no remixing by convection can be expected, as the denser fluid is at the bottom).

The liquid sample is a circular, horizontal slab 38 mm in diameter and 4.50 mm thick. It is confined between two thick sapphire plates (chosen for their relatively good thermal conductivity), and the temperature is controlled to better than 1 mK. A 5 mK stabilizing temperature difference between top and bottom plates is maintained to discourage stray convection across the slab. In the set-ups

for both shadowgraphs and light scattering, the optical axis is vertical.

An image-forming white-light shadowgraph<sup>9</sup> was used to form images of the fluid slab. We show in Fig. 1 a sequence of pictures obtained in the two-phase situation below  $T_c$  and at various intervals from seconds to days after the temperature jump above  $T_c$ . Regular and uniform fluctuations appear shortly after the temperature jump into the one-phase region and they decrease in amplitude as time goes on, as shown by the loss of contrast. Eventually, the system falls back to an optically homogeneous state, similar to that before the temperature jump (see Fig. 1a, f). When observed live, the patterns fluctuate with a typical time constant of the order of one second. Although largely qualitative in nature, the shadowgraph images give an estimate of the spatial extent of the fluctuations, which grow to a macroscopic level. A characteristic length is about 70  $\mu\text{m}$  (Fig. 1b).

Static light scattering was used to determine the amplitude of the concentration fluctuations as a function of the scattering wave-vector  $q = (4\pi/\lambda)n \sin(\theta/2)$ , where  $\theta$  is the scattering angle,  $\lambda$  is the wavelength of the probe beam and  $n$  is the refractive index of the mixture. We present data obtained with an ultra-low-angle light-scattering apparatus<sup>10</sup>, which covers a range of angles  $2' < \theta < 3^\circ$ , corresponding to a  $q$ -vector range  $84 \text{ cm}^{-1} < q < 7,850 \text{ cm}^{-1}$ .

We show in Fig. 2 a sequence of scattered intensity distributions as a function of  $q$ , taken at various times after the beginning of the diffusion process. The strongest scattering occurs for the first set (circles in Fig. 2) obtained immediately after the quench into the one-phase region. The scattered intensity diverges as  $q$  is reduced, but the curves eventually saturate at a constant value at smaller  $q$ . We have also plotted (dashed line) the scattered intensity from equilibrium fluctuations,  $I_{\text{eq}} \propto (\partial n/\partial c)^2 (\partial c/\partial \mu)$ , is the chemical potential as estimated from turbidity measurements<sup>11</sup> and according to the procedure explained in ref. 12. A substantial enhancement of the fluctuations by a few orders of magnitude can be clearly seen (despite this, however, the integrated effect leads to small changes in turbidity<sup>13</sup>).

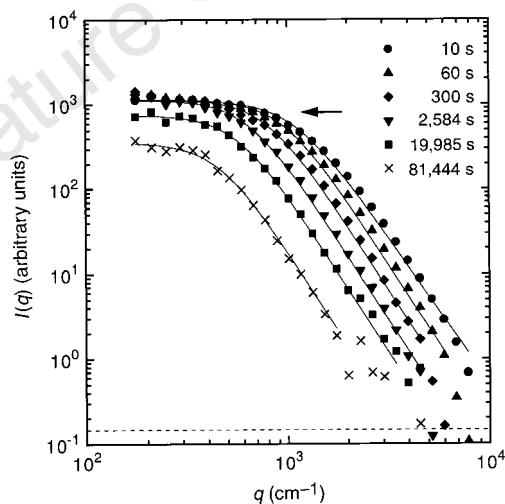


**Figure 2** Non-equilibrium scattered intensity distributions plotted as a function of the wavevector  $q$  at different times during the diffusion process. The values for the elapsed time have been corrected to account for the finite time required to establish a uniform temperature across the cell (roughly 80 s). The solid line through the data is their best fit with equation 1. The dashed line is the reference equilibrium intensity scattered by the sample in its homogeneous state at  $T - T_c = 1$  K. The turbidity originated from equilibrium fluctuations corresponds<sup>11</sup> to  $\tau \approx 5 \times 10^{-2} \text{ cm}^{-1}$ . The arrow marks the level of the non-equilibrium forward-scattered intensity as calculated from equation 3.

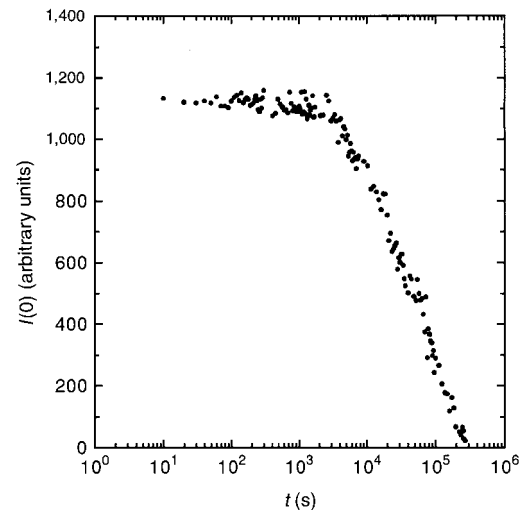


**Figure 3** Forward-scattered intensity as a function of the time elapsed after the start of the diffusion process. The sudden drop in  $I(0)$ , which occurs for  $t \approx 4,000$  s, corresponds to the transition from free diffusion behaviour (where the concentration profile evolves as if the sample were infinite in the vertical direction) to the restricted diffusion behaviour (the presence of impermeable boundaries influences the evolution of the concentration profile).

Theories of fluctuating hydrodynamics<sup>14</sup> have been developed in connection with steady-state non-equilibrium fluctuations<sup>4-6,15,16</sup>. Experimental data verifying these theories have been presented previously<sup>12,17-20</sup>. The calculations of ref. 16 can be extended (A.V. and M.G., manuscript in preparation) to treat the time-dependent case of free diffusion and to calculate the scattered intensity distribution from an isothermal layer of fluid characterized by a concentration gradient  $\nabla c$ . The non-equilibrium scattered intensity is given by

$$I(q, t) \propto \left(\frac{\partial n}{\partial c}\right)^2 \frac{1}{\nu D} \frac{1}{1 + \left(\frac{q_{ro}}{q}\right)^4} \frac{(\nabla c)^2}{q^4} \quad (1)$$

where  $\nu$  is the kinematic viscosity and  $D$  is the mass diffusion coefficient. Equation 1 describes the fast  $q^{-4}$  divergence at large  $q$  that is characteristic of non-equilibrium fluctuations that originate from the coupling between velocity fluctuations and concentration fluctuations<sup>4-6,15-20</sup>. This is the same mechanism that gives rise to the large non-equilibrium fluctuations described in ref. 12. Equation 1 also describes the saturation at low  $q$ , where, as we will discuss later, any dependence on non-trivial fluid parameters actually cancels out. The transition between the two asymptotic behaviours occurs at the roll-off wavevector  $q_{ro}$  given by

$$q_{ro} = \left(\frac{\beta g \nabla c}{\nu D}\right)^{1/4} \quad (2)$$

where  $\beta = \rho^{-1}(\partial \rho / \partial c)_{p,T}$ , where  $\rho$  is the mass density and  $g$  is the gravitational acceleration.

The continuous lines through the data in Fig. 2 have been fitted according to equation 1 by floating the roll-off position and the asymptotic  $I(q \approx 0)$  value. Best fitting of the asymptotic behaviour at large  $q$  was obtained by slightly changing the power-law dependencies in equation 1 (an exponent of 3.7 was used instead of 4).

The scattered intensity at small  $q$ ,  $I(q \approx 0)$ , remains constant at first, but then it drops steadily. This behaviour is shown in detail in Fig. 3. If roughly the scattered intensity from the various layers of fluid is integrated (see equation 1), the overall scattered intensity at  $q = 0$  becomes

$$I(q = 0) \propto \left(\frac{\partial n}{\partial c}\right)^2 \frac{\Delta c}{\beta g} \quad (3)$$

where  $\Delta c$  is the difference between the concentrations of the uppermost and lowermost layers of the sample. During the early

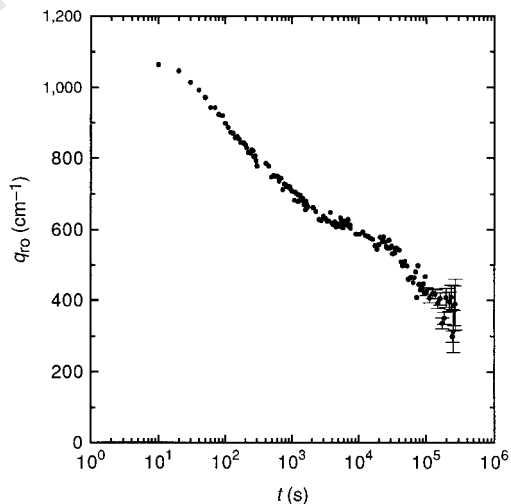


**Figure 4** Roll-off wavevector  $q_{ro}$  as a function of time. The wavevector slowly decreases with time, indicating that fluctuations inside the sample grow larger as time goes by.

phases the diffusion proceeds mostly around the midplane, and  $\Delta c$  is constant (free diffusion regime). Later on the limitations of a restricted geometry are felt, and  $\Delta c$  diminishes steadily<sup>21</sup>, producing the behaviour shown in Fig. 3. The time at which the break in Fig. 3 occurs can be used to derive an estimate of the diffusion coefficient  $D = (1.5 \pm 0.3) \times 10^{-6} \text{ cm}^2 \text{ s}^{-1}$ . An estimate for  $D$  from reference data<sup>22,23</sup> along the critical isotherm at  $\delta c \approx 0.5$  gives  $D = 1.8 \times 10^{-6} \text{ cm}^2 \text{ s}^{-1}$ . Incidentally, the time constant  $\tau$  associated with the fluctuations of the shadowgraph images (1 second) compares nicely with the estimate  $\tau = 1/(Dq_{ro}^2)$ . As  $\Delta c = \delta c = 0.5$  and  $\beta = 0.27$ , we are in a position to calculate the theoretical value of the non-equilibrium forward-scattered intensity, relative to the equilibrium value. The value is shown in Fig. 2 by an arrow, and the agreement with the experimental data is within 40%, good agreement considering the uncertainty in reference data for  $(\delta c / \delta \mu)$ .

We emphasize that equation 3 shows that the low- $q$  fluctuation amplitude does not depend on any relevant fluid parameter. So the orders-of-magnitude increase of the fluctuations above the equilibrium value (the most prominent feature that can be captured experimentally) is to be expected for any non-equilibrium fluid that has macroscopic concentration variations comparable to those in this experiment.

The roll-off position does depend on the transport coefficients  $\nu$  and  $D$ . The time dependence of  $q_{ro}$  is shown in Fig. 4. It is known that during free, unbounded diffusion the concentration gradient at the midheight scales with the inverse square root of time<sup>3</sup>. From equation 2 then it follows that  $q_{ro} = q_1 t^{-1/8}$ , where the prefactor can be estimated from reference data (using our own determination  $D = 1.5 \times 10^{-6} \text{ cm}^2 \text{ s}^{-1}$ ) to be  $q_1 = 1.1 \times 10^3 \text{ cm}^{-1} \text{ s}^{1/8}$ . The best fit of the data in Fig. 4 yields an exponent  $-0.11 \pm 0.01$  and a prefactor  $q_1 = (1.5 \pm 0.06) \times 10^3 \text{ cm}^{-1} \text{ s}^{1/8}$ . The agreement is satisfactory. The value of  $q_{ro}$  determines the largest wavelength at which the effects of the gravity are not felt<sup>12,16</sup>. For lower  $q$  vectors the strong  $q^{-4}$  divergence is cut off. We must stress that the roll-off depends on  $g$ , and by reducing it the strong divergence becomes operative at longer wavelengths. We point out that in space experiments where  $g$  is really small, very large effects should be expected.

Equation 1 predicts that in the  $q^{-4}$  regime the scattered intensity scales as  $(\nu D)^{-1}$ . Consequently the choice of a near-critical fluid is advantageous in the large- $q$  regime. For ordinary liquids  $D \approx 10^{-5} \text{ cm}^2 \text{ s}^{-1}$  and therefore a factor of roughly ten is gained.

Finally, we point out that this work has strong connections with the area of convective instabilities, with special reference to the two-component Rayleigh-Bénard instability, where a temperature gradient is applied to a fluid slab<sup>24,25</sup>. There too velocity and concentration modes couple, and large fluctuations are generated before the onset of the instability. Clear evidence of large pretransitional fluctuations has been presented<sup>26</sup>. Indeed, it has been shown<sup>15,16</sup> that the physical mechanism that leads in our case to the divergence cutoff is the same (but with opposite effects) as that which determines the instability threshold in the Rayleigh-Bénard case. □

Received 2 April; accepted 25 September 1997.

1. Tanford, C. *Physical Chemistry of Macromolecules* (Wiley, New York, 1961).
2. Tyrrtel, H. J. V. *Diffusion and Heat Flow in Liquids* (Butterworths, London, 1961).
3. Cussler, E. L. *Mass Transfer in Fluid Systems* (Cambridge Univ. Press, 1984).
4. Kirkpatrick, T. R., Cohen, E. G. D. & Dorfman, J. R. Light scattering by a fluid in a nonequilibrium steady state. II. Large gradients. *Phys. Rev. A* **26**, 995-1014 (1982).
5. Ronis, D. & Procaccia, I. Nonlinear resonant coupling between shear and heat fluctuations in fluids far from equilibrium. *Phys. Rev. A* **26**, 1812-1815 (1982).
6. Law, B. M. & Nieuwoudt, J. C. Noncritical liquid mixtures far from equilibrium: The Rayleigh line. *Phys. Rev. A* **40**, 3880-3885 (1989).
7. Berge, P., Calmettes, P., Laj, C., Tournarie, M. & Volochine, B. Dynamics of concentration fluctuations in a binary mixture in the hydrodynamical and nonhydrodynamical regimes. *Phys. Rev. Lett.* **24**, 1223-1225 (1970).
8. Atack, D., Rice, O. K. The interfacial tension and other properties of the cyclohexane + aniline system near the critical solution temperature. *Discuss. Faraday Soc.* **15**, 210-218 (1953).
9. de Bruyn, J. R. *et al.* Apparatus for the study of Rayleigh-Bénard convection in gases under pressure. *Rev. Sci. Instrum.* **67**, 2043-2067 (1996).
10. Carpinetti, M., Ferri, F., Giglio, M., Paganini, E. & Perini, U. Salt-induced fast aggregation of polystyrene latex. *Phys. Rev. A* **42**, 7347-7354 (1990).

11. Calmettes, P., Laguès, I. & Laj, C. Evidence of nonzero critical exponent  $\eta$  for a binary mixture from turbidity and scattered light intensity measurements. *Phys. Lett. Lett.* **28**, 478–480 (1972).
12. Vailati, A. & Giglio, M.  $q$  divergence of nonequilibrium fluctuations and its gravity-induced frustration in a temperature stressed liquid mixture. *Phys. Rev. Lett.* **77**, 1484–1487 (1996).
13. Vailati, A. & Giglio, M. Study of the  $q$  divergence of nonequilibrium fluctuations in a stressed fluid. *Physica A235*, 105–109 (1997).
14. Landau, L. D. & Lifshitz, E. M. *Fluid Mechanics* (Pergamon, New York, 1959).
15. Segrè, P. N., Schmitz, R. & Sengers, J. V. Fluctuations in inhomogeneous and nonequilibrium fluids under the influence of gravity. *Physica A195*, 31–52 (1993).
16. Segrè, P. N. & Sengers, J. V. Nonequilibrium fluctuations in liquid mixtures under the influence of gravity. *Physica A198*, 46–77 (1993).
17. Law, B. M., Gammon, R. W. & Sengers, J. V. Light-scattering observations of long-range correlations in a nonequilibrium liquid. *Phys. Rev. Lett.* **60**, 1554–1557 (1988).
18. Segrè, P. N., Gammon, R. W., Sengers, J. V. & Law, B. M. Rayleigh scattering in a liquid far from thermal equilibrium. *Phys. Rev. A45*, 714–724 (1992).
19. Segrè, P. N., Gammon, R. W. & Sengers, J. V. Light scattering measurements of nonequilibrium fluctuations in a liquid mixture. *Phys. Rev. E47*, 1026–1034 (1993).
20. Li, W. B., Segrè, P. N., Gammon, R. W. & Sengers, J. V. Small-angle Rayleigh scattering from nonequilibrium fluctuations in liquids and liquid mixtures. *Physica A204*, 399–436 (1994).
21. Crank, J. *The Mathematics of Diffusion* (Oxford Univ. Press, New York, 1975).
22. Stanley, H. E. *Introduction to Phase Transitions and Critical Phenomena* (Oxford Univ. Press, New York, 1971).
23. Giglio, M. & Vendramini, A. Thermal-diffusion measurements near a consolute critical point. *Phys. Rev. Lett.* **34**, 561–564 (1975).
24. Chandrasekar, S. *Hydrodynamic and Hydromagnetic Stability* (Clarendon, Oxford, 1961).
25. Normand, C., Pomeau, Y. & Velarde, M. G. Convective instability: A physicist's approach. *Rev. Mod. Phys.* **49**, 581–624 (1977).
26. Wu, M., Ahlers, G. & Cannell, D. S. Thermally induced fluctuations below the onset of Rayleigh-Bénard convection. *Phys. Rev. Lett.* **75**, 1743–1746 (1995).

**Acknowledgements.** This work was partially supported by ASI (Agenzia Spaziale Italiana).

Correspondence and requests for materials should be addressed to M.G. (e-mail: giglio@mi.infn.it).

## A manganese oxyiodide cathode for rechargeable lithium batteries

Jaekook Kim & Arumugam Manthiram\*

Center for Materials Science and Engineering, ETC 9.104, The University of Texas at Austin, Austin, Texas 78712, USA

The increasing demand for portable electronic devices is driving the development of compact lightweight batteries of high energy density<sup>1</sup>. Lithium-ion batteries tend to be the systems of choice, as they offer higher energy densities and longer operational lifetimes than other rechargeable battery systems<sup>1,2</sup>. But commercially available lithium-ion batteries make use of layered LiCoO<sub>2</sub> cathodes<sup>3,4</sup>, and the high cost and toxicity of cobalt therefore motivate the development of cheaper and environmentally benign cathode materials. In this regard, manganese oxides are attractive alternatives, and the spinel LiMn<sub>2</sub>O<sub>4</sub> has been investigated intensively as a cathode<sup>5,6</sup>; however, the fading on cycling of its energy-storage capacity poses problems. More recently, attention has been focused on the synthesis of layered LiMnO<sub>2</sub> as a cathode material, but its cycling characteristics remain to be established<sup>7–9</sup>. Here we report the synthesis and electrochemical performance of a new manganese oxide cathode, the oxyiodide Li<sub>1.5</sub>Na<sub>0.5</sub>MnO<sub>2.85</sub>I<sub>0.12</sub>. Our material exhibits a high reversible capacity of 260 mA h g<sup>-1</sup> in the range 1.5–4.3 V with excellent cycling characteristics. Furthermore, the amorphous nature of the material (as determined by X-ray diffraction) and smooth discharge behaviour may help to overcome the problems associated with lattice distortions that have plagued manganese oxides with more crystalline structures<sup>5–9</sup>.

Complex metal oxides are traditionally made by repeated grinding and firing of the raw materials at high temperatures in order to overcome the diffusional limitations. Such a 'brute force' high-temperature approach often leads not only to larger grain size and lower surface area, but also to an inaccessibility of metastable phases that may have unusual valences or atomic arrangements. This

awareness has created tremendous interest in designing low-temperature routes to synthesize complex materials<sup>10</sup>. We have shown<sup>11</sup> that alkali metal borohydrides such as NaBH<sub>4</sub> can be used effectively to reduce metalate ions (MO<sub>3</sub>)<sup>2-</sup> (where M is V, Mo or W) in aqueous solutions to obtain binary oxides M<sub>2</sub>O<sub>3</sub> and ternary oxides Na<sub>x</sub>M<sub>2</sub>O<sub>z</sub>. The method gave amorphous or nanocrystalline phases, which were often metastable, and the binary oxides such as VO<sub>2</sub> and MoO<sub>2</sub> obtained by this approach were found to be attractive as electrode materials for lithium batteries<sup>12,13</sup>.

Here we use LiI as a reducing agent to reduce the permanganate ion (MnO<sub>4</sub>)<sup>-</sup> in acetonitrile medium. The use of a non-aqueous medium is particularly important to obtain electrode materials free from water. NaMnO<sub>4</sub>·H<sub>2</sub>O was heated at 170 °C for 2 hours to obtain anhydrous NaMnO<sub>4</sub>. A 0.05-M NaMnO<sub>4</sub> solution was then prepared by dissolving the anhydrous NaMnO<sub>4</sub> in acetonitrile. Anhydrous LiI was then added under constant stirring to the NaMnO<sub>4</sub> solution so that the molar ratio of NaMnO<sub>4</sub> to LiI is 1:1.5. After the mixture had been kept under constant stirring for about 1 day, the solid formed was filtered and washed several times with acetonitrile to remove the iodine formed during the reduction process.

The as-prepared sample was found to be amorphous to X-ray diffraction (Fig. 1a). The sample was then heated in vacuum at 250 °C for about 10 h to remove the residual solvent acetonitrile or any adsorbed water before preparing the electrodes. The vacuum-annealed sample also did not show any sharp reflections (Fig. 1b), indicating that the sample was still amorphous to X-ray diffraction. However, after the sample had been annealed in air or N<sub>2</sub> atmosphere at a temperature  $T > 300$  °C, reflections corresponding to Li<sub>2</sub>MnO<sub>3</sub> and a small amount of Na<sub>0.7</sub>MnO<sub>2</sub> were observed in the X-ray diffraction pattern (Fig. 1c). Figure 2 shows a micrograph recorded with a Jeol 200 CX transmission electron microscope (TEM), along with the selected area diffraction (SAD) pattern for the vacuum-annealed sample. The SAD pattern shows very diffuse rings, suggesting that the sample is not totally amorphous. It implies that short-range order may exist on the length scale of a few Mn–O polyhedra, which is not a long enough range to give well-defined diffraction patterns. This conclusion is also consistent with the development of a few broad reflections in the X-ray pattern of the vacuum-annealed sample (Fig. 1b) that are reminiscent of Li<sub>2</sub>MnO<sub>3</sub> reflections.

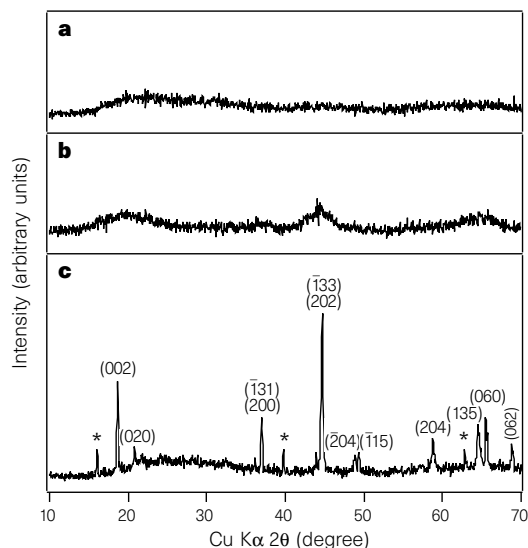


**Figure 1** X-ray powder diffraction patterns of the product obtained by reducing permanganate with LiI. **a**, As prepared; **b**, after heating in vacuum at 250 °C; and **c**, after heating in air at 600 °C. The planes marked in **c** refer to Li<sub>2</sub>MnO<sub>3</sub> and the asterisk refers to Na<sub>0.7</sub>MnO<sub>2</sub>.